



## Synthesis, Characterizations and Optimization of Magnesium Oxide Scaffold for Bone Healing Applications

Lamyaa Hadi Mohammed

Department of Human Anatomy, Section Histology and embryology, College of Medicine, Al-Nahrain University, Baghdad, Iraq.

### Article's Information

Received: 19.04.2024  
Accepted: 14.05.2024  
Published: 15.06.2024

**Keywords:**  
MgO  
Nanoparticles  
Structure  
Optical Properties

### Abstract

In this work, the structural properties of Magnesium oxide nanoparticles (MgO NPs) are synthesized by a simple chemical technique. X-ray diffraction pattern (XRD) pattern showed the crystalline nature of MgO NPs. The average diameter of MgO NPs calculated by SEM and XRD was around 19 nm. Energy dispersive X-ray spectroscopy (EDS) spectrum and XRD pattern suggested that prepared MgO NPs were highly pure. The viability of cells in a medium containing MgO-AV composite scaffold was nearly equal to that of MgO, AV, and control, with no statistically significant difference ( $p > 0.05$ ). The Runx2-mediated modulation of gene expressions of the bone biomarkers ALP and OCN was investigated to determine the mechanism of scaffold-induced improvement in bone repair. ALP was immunodetected in the injured site of the right femur twenty-one days after the bone defects were created. The implantation of scaffolds into the bone defect region of the left femur, on the other hand, resulted in a noticeable increase in ALP levels. Similarly, OCN was immunodetected in the right femur's bone defect site. The implantation of scaffolds into the bone defect location of the left femur, on the other hand, resulted in a significant increase in OCN levels. The low-level diode laser therapy (LLLT) promotes the partially bony incorporation of the xeno bony implantation with the recipient femoral bone, and can successfully fill the space, and support the weight after removing the internal fixation methods, with no body rejection. The histopathological finding at the end of the 6th week post-operation in treatment groups the trabecular bone is mature and wide with little cavity. The control group showed immature and thin trabecular bone, with large cavities, and an area of connective tissues not organized. At the end of 12th weeks, post-operation the treatment groups revealed mature trabecular bone surrounding the bony device and lamellar bone formation with partial bony incorporation, the lacuna and haversian canals of the bony device filled with osteocyte and blood vessels, while in control groups the trabecula bone not mature, and many lacuna and havesan canal still empty in the bony device.

<http://doi.org/10.22401/ANJS.27.2.12>

\* Corresponding author: [lamyahadi2016@gmail.com](mailto:lamyahadi2016@gmail.com)



This work is licensed under a [Creative Commons Attribution 4.0 International License](https://creativecommons.org/licenses/by/4.0/)

### 1. Introduction

In recent years, nanoscience and technology have emerged as significant disciplines in the scientific community [1]. Nanotechnology has played a crucial role in the industrial revolution, focusing on the creation of structured materials that exhibit improved properties compared to their intrinsic aspects [2]. The shape, size, composition, and lattice

structure of nanomaterials greatly influence their properties. The utilization of nanoscale structures allows for specific size configurations, which are essential for achieving consistent material responses [3]. Apart from hydrothermal and precipitation methods, microemulsion methods have also been utilized for producing nanoparticles from aqueous solutions [4-6]. Wet chemical synthesis of

nanoparticles finds applications in various areas, including industrial applications and as alternatives to conventional processes and gas phase synthesis [7]. In recent years, there has been significant interest in inorganic materials such as metals and metal oxides due to their ability to withstand extreme operating conditions [8, 9]. Metal oxides, such as titanium dioxide, zinc oxide, and magnesium oxide, have gained attention for their stability and reputation as safe materials for both humans and animals [10]. At low concentrations, metals and metal salts can exhibit toxicity toward microorganisms by binding to intracellular proteins and rendering them inactive [11]. Silver and zinc oxide nanoparticles have shown promise in preventing infectious diseases due to their strong antimicrobial properties. The growing concerns regarding health and customer satisfaction have driven rapid advancements in the field of functional finished textiles [12]. Magnesium oxide, with its wide range of applications in catalysis, adsorption, and the synthesis of refractory ceramics, is an intriguing basic oxide [13-16]. Its high ionic character, simple structure, and stoichiometry make it suitable for various purposes.

## 2. Materials and Methods

### 2.1. MgO NPs

Magnesium oxide nanoparticles were prepared with simple chemical technology using Magnesium chloride ( $MgCl_2$ , NaOH) as the filtered water state is not ionic. Then the solution was kept. The contents are completely thawed under constant stirring with a magnetic stirrer at room temperature.

### 2.2. Preparation of MgO Scaffolds

MgO scaffolds were cut to a diameter of 5 mm and a thickness of 3 mm for the studies. The scaffolds were disinfected in 70% ethanol for 30 minutes before being subjected to UV radiation for another 30 minutes on each side.

To separate the water-soluble fraction (rich in acetylated polysaccharides) from the cellulose-rich solid fraction, commercial aloe vera juice was centrifuged at 3000 rpm for 15 minutes. The water-soluble fraction (supernatant) was utilized to coat the structures, and it contains bioactive polysaccharides, phenolic compounds, soluble carbohydrates, proteins, and minerals, in addition to the bioactive polysaccharides. The pH of the supernatant is around 4. The presence of several

organic acids can explain the extracts' somewhat acidic nature (acetic acid, lactic acid, succinic acid, etc.). Through pH modification, three types of aloe vera extract samples were obtained: a pH 3 solution (adjusted with 0.018 M HCl), a pH 5 solution (adjusted with 0.5 M NaOH), and the pH 4 gel as obtained.

Each scaffold was immersed in 1 mL of aloe vera extract solution and agitated for 3 hours, allowing interaction between the functional groups generated on the scaffolds' surface and the functional groups in the polysaccharides' structures to occur. After that, the samples were washed with 70% ethanol to eliminate any remaining aloe vera that had failed to adhere to the surface. In addition, because polysaccharides are insoluble in ethanol, their precipitation aids in the adhesion of the coating to the surface scaffolds.

### 2.3. Animals

The animals were obtained from the National Center for Drug Control and Research (NCDCR), an organization affiliated with the Ministry of Health. This affiliation guarantees a flawless trial. Before the procedure, the rabbits were kept in specialized cages for seven days. Additionally, all animals were given a dose of antiparasitic medicine (Ivermectin 0.1 mg/kg) to prevent both internal and external parasites. Afterward, a surgical transverse fracture was created near the mid-shift of the femoral bone, resulting in the removal of approximately 1cm of length. Subsequently, the animals were divided into four equal groups. The femoral gap was filled with a scaffold implant of appropriate size, which was secured using an intramedullary pin as an internal fixation device. Each group consisted of 40 rabbits, with one group acting as the control and the other as the treatment group. Before the surgery, all instruments, towels, and equipment underwent autoclaving at a temperature of 121 degrees Fahrenheit and a pressure of 20 bars for 30 minutes.

### 2.4 Anesthesia and creation of bone fracture

Before the procedure, the rabbits underwent 12 hours without food and 2 hours without water. General anesthesia was induced by administering intramuscular injections of 2 percent xylazine hydrochloride (17.5 mg/kg), 5 percent ketamine hydrochloride (25 mg/kg), and 0.5 cc lidocaine at the incision site. The dosage of antibiotics and

anesthetics was calculated using the formula provided.

$$Dose = \frac{Animal\ weight \times dose\ rate}{Concentration\ of\ drug} \dots (1)$$

The surgical site on the thigh was meticulously prepared for a highly sterile procedure. This involved cutting, shaving, washing with soap and water, and disinfecting with 70% alcohol from the hip joint to the stifle joint. All necessary equipment, such as surgical tools, sutures, an electrical saw, curtains, goggles, and gloves, was brought in. The goal of this phase was two-fold: first, to remove a 1cm section of the femoral bone, and second, to create a scaffold for implantation to fill the void in the thigh. The scaffold was internally fixed using a binding device. The experiment was conducted on a group of 40 healthy adult rabbits, weighing between 2-2.5 kg and aged 12 to 18 months.

## 2.5. Surgical Protocol

After the administration of anesthesia, the animals were positioned in lateral recumbency. A sterile surgical drape covered the entire body, except for the surgical area. The surgical field was prepared by applying alcohol-soaked cotton and 2% iodine tincture. A surgical incision of approximately 4 cm was made on the lateral thigh, extending from the greater trochanter to the lateral side of the patella. Hemostasis was performed as part of the routine procedure. The subcutaneous tissue was dissected, followed by a sharp dissection of the fascia lata. The biceps femoris and biceps femoris muscles were then separated to expose the mid-displacement of the femur. The abducted muscle was carefully separated from the femur bone at the fracture site using curved and fine artery forceps. To protect the surrounding soft tissues, two curved scissors were used, and an electrical saw was employed to remove approximately 1 centimeter of the femoral shaft. Throughout this process, sterile normal saline was used to cool the bone. Afterward, the two femoral bone pieces with the scaffold implantation were internally fixed using intramedullary pins with a diameter of 2.5–2.25 mm. These pins were implanted in the femoral empty defect space once the appropriate-sized scaffold was placed. The muscles and fascia lata were sutured using a simple continuous pattern with 2/0 chromic catgut individually. The skin was closed using a simple interrupted pattern with 2/0 non-absorbable silk materials. The pins were inserted using a retrograde pin choke technique, and penicillin

powder was applied locally as an antibiotic. Following the treatment, the excess length of the pin should be cut with a pin cutter as soon as possible to ensure proper placement and alignment of the intramedullary pins and their bone implantation [12–22].

## 3. Result and Discussion

The XRD pattern presented in Figure 1 illustrates the sample prepared through the wet chemical method. This pattern reveals the presence of impurities and inadequate calcination temperatures, as evidenced by the broad, unexplained peaks observed in the XRD pattern of the MgO nanoparticles synthesized at 400°C and 500°C. However, upon increasing the calcination temperatures to 700°C and 800°C, the peaks became sharper and no unidentified peaks were observed. This suggests that pure nanocrystalline MgO was formed without any foreign components, and the crystallinity of the material improved. The crystal structure of the MgO nanoparticles was determined using X-ray diffraction (XRD). The size and crystallinity of the particles can be inferred from the width and intensity of the peaks. The XRD pattern of the produced MgO sample (Fig. 2) displays five visible peaks at 19.02, 29.70, 38.31, 51.11, and 59.98. By employing the Debye-Scherrer equation, the average particle size of the nanoparticles was calculated to be 22 nanometers.

The scanning electron microscopy image in Fig. 2 illustrates the synthesized MgO nanoparticles. At 400x magnification and a temperature of 700°C, the micrograph displays distinct particles with a particle-like structure that is easily discernible. These particles are uniformly dispersed in the sample, with some being closely associated or connected. The examination of the MgO nanoparticles through scanning electron microscopy, as displayed in Fig 2 (a, b), showcased distinct particles when observed at magnifications of 400 and 700°C. When magnesium hydroxide is heated to 400 degrees Celsius, it results in the production of compact flakes. However, increasing the temperature to 600 degrees Celsius causes the flakes to transition into isometric particles with irregular shapes. At 700°C, the aggregates exhibit irregular shapes.

The transmittance and absorbance spectra were employed to analyze the optical characteristics of

MgO nanoparticles over a wavelength range of 200-900 nm. The transmittance spectrum of MgO nanoparticles in Fig. 3 illustrates a rising pattern with increasing wavelength. In contrast, Fig. 4 illustrates the absorbance spectrum, showing an opposite trend to transmittance as the absorbance diminishes with increasing wavelength. The optical energy gap of MgO nanoparticles is shown in Fig. 5, with a determined value of 4 eV.

Bone histomorphometry was performed to illustrate the improvement in bone regeneration within damaged areas facilitated by the scaffolds. Twenty-one days after the creation of the bone defect, there was clear evidence of new trabecular bone formation at the femur defect site. The introduction of scaffolds into the defect site resulted in a notable increase in the generation of new trabecular bone when compared to the control group. Upon histopathological evaluation after of the 6th-week post-surgery in the treatment groups, there was a noticeable rise in mature, wide, and well-mineralized trabecular bone formation with minimal cavities present. In contrast, the control groups displayed thin trabecular bone with lower mineralization and larger cavities. By the end of the

12th-week post-surgery in the treatment groups, there was observable mature trabecular bone formation, well mineralized, widening, and lamellar bone formation surrounding the bony device, in addition to partial bone integration. The empty osteocyte lacuna of the bony device was filled with osteocytes, and blood vessels had infiltrated the haversian canal. In contrast, the control groups exhibited slender trabecula bone, reduced mineralization, and numerous cavities. Additionally, some empty lacunae within the bony device remained unfilled with osteocytes, resulting in an enlargement of the haversian canal diameters. The physical and mechanical analyses indicated that the treatment group displayed higher density and hardness in comparison to the control group. Furthermore, when subjected to pressure and heat for fracture tolerance analysis, the treatment group showcased enhanced resistance to pressure and superior fracture tolerance as opposed to the control group. The histopathological findings of the control group unveiled that 70% of the implanted bony device did not undergo conversion into active or living bone, as the empty lacunae were not filled with active osteocytes.

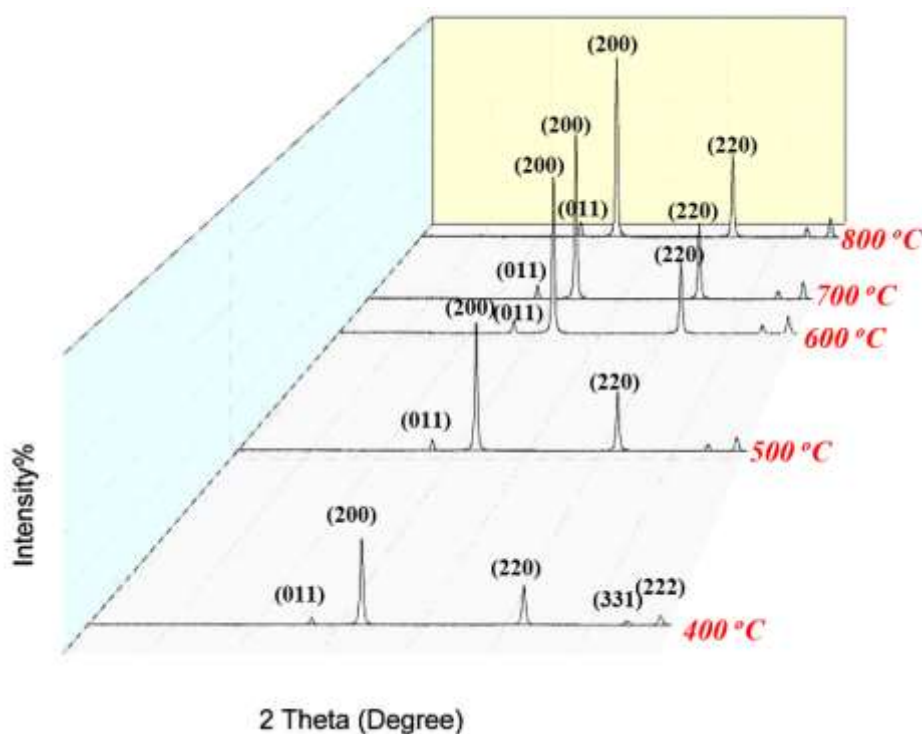
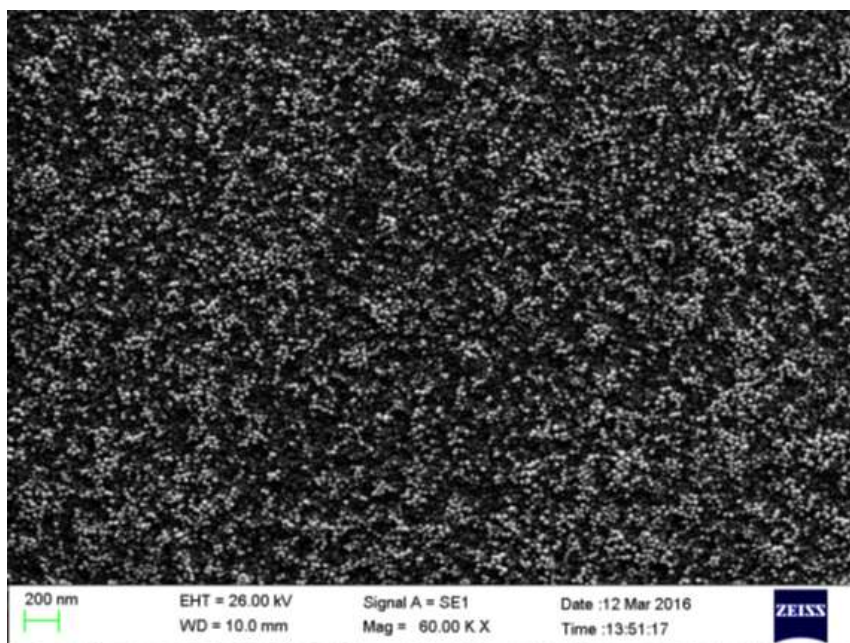
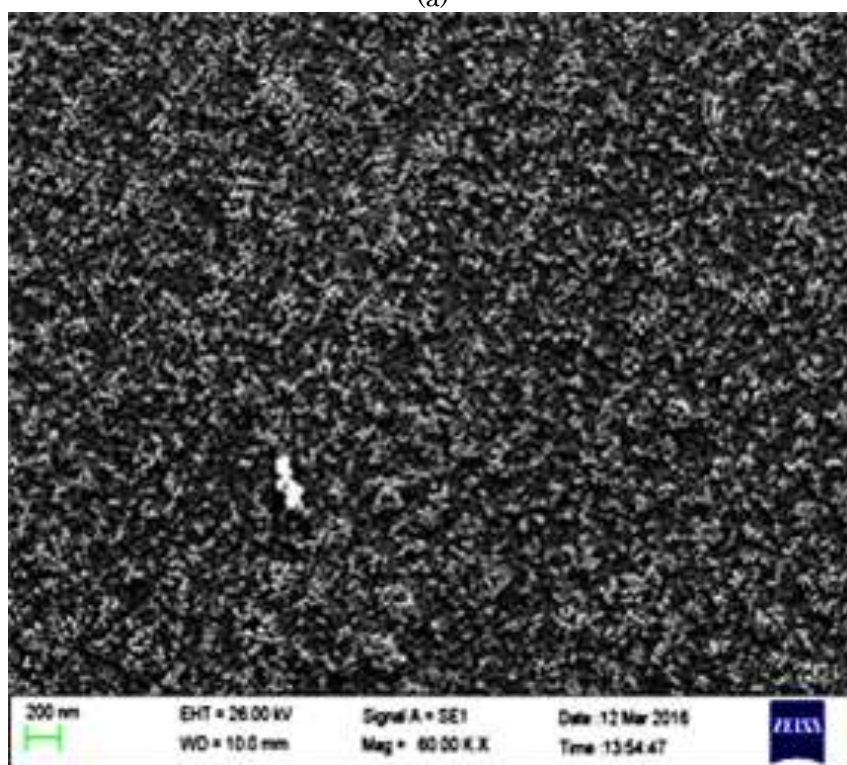


Figure 1. XRD spectrum of MgO nanoparticles at three calcination temperature.



(a)



(b)

Figure2. SEM images of MgO nanoparticles at three calcinating temperature.

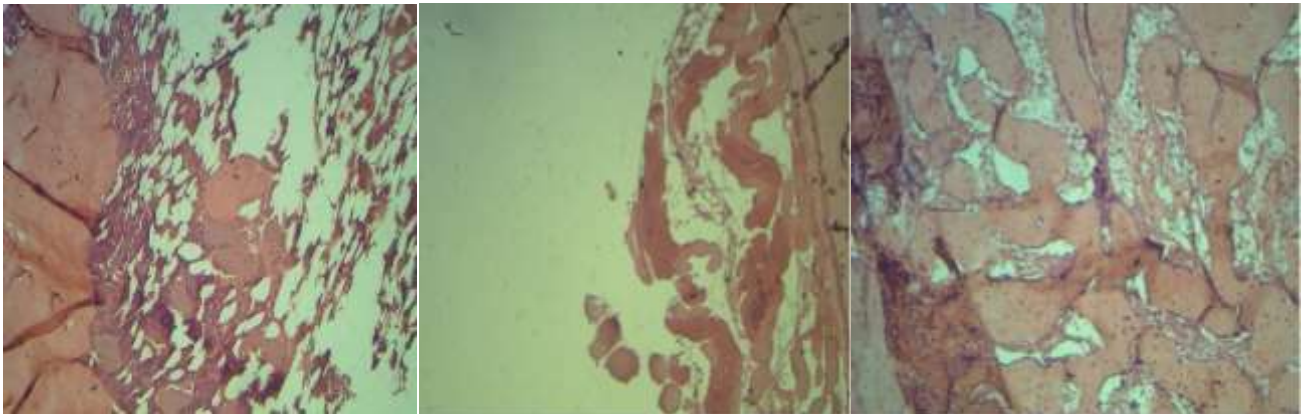


**Figure 6.** Effect of Scaffolds on Bone Healing using Bone Histological.

The examination of histopathology performed 6 weeks post-operation in the treatment groups displayed an augmentation in trabecular bone formation. The bone was observed to be mature, wide, and well mineralized, with only a small cavity within the trabeculae. Conversely, the control groups showcased thin and poorly mineralized trabecular bone with large cavities (fig. 6). Following 12 weeks post-operation, the treatment groups exhibited mature trabecular bone formation that was well mineralized, widened, and had lamellar bone formation surrounding the bony device. Moreover, there was partial bone incorporation, with the empty osteocyte lacuna of the bony device being filled with osteocytes and blood vessels invading the haversian canal. In contrast, the control groups had a thin trabecular bone that was less mineralized, with numerous cavities. The trabecular bone did not transition to the lamellar bone, and some of the empty lacuna within the bony device remained unfilled with osteocytes. Additionally, there was an increase in the diameters of the haversian canal (fig. 6). All the physical and mechanical analyses conducted indicated that the treatment group displayed higher density and hardness in comparison to the control group. When subjected to pressure and heat for fracture tolerance analysis, the results suggested that the treatment group exhibited greater resistance to pressure and could withstand the fracture test more effectively than the control group. The unoccupied area within the bony structure, where active osteocytes were not fully present according to histopathological examination in the control group, demonstrated that 70% of the implanted bony structure did not convert into active

or living bone. In the treatment group, low-level diode laser therapy (LLLT) accelerates the formation of new bone tissue, resulting in enhanced metabolism and mineralization in the initial phases of bone healing. This is accomplished by stimulating bone growth and increasing its density through mineralization activity. The physical properties of laser energy expedite the mending of fractures, encourage the formation of calluses, promote new blood vessel growth at the fracture site, improve the deposition of collagen fibers, and enhance the proliferation of bone cells. The high level of blood supply between the bone fragments and the bony structure allows for blood vessels to penetrate the bony structure, leading to rapid integration of bone and the ability to support weight and fill the empty space defect even after the pins are removed. This is corroborated by various sources indicating that the revascularization and osteoinduction phase plays a critical role in bone integration and gradual replacement, achieved by blood vessels penetrating the bony structure to fill the spaces and Haversian canals, which may vary depending on the type of graft or implant utilized. Low-level diode laser therapy (LLLT) expedites the bone healing process, especially in the early stages of bone formation, and significantly improves the mechanical strength of newly formed bone tissues by enhancing blood supply, organizing collagen fibers, and expediting the healing of bone defects. Furthermore, the laser has beneficial effects on bone metabolism and fracture healing, accelerating the repair process and increasing the volume of calluses and bone mineral density. Xenogeneic bony implantation was employed to fill the space, provide support for

weight-bearing, and act as a source of calcium and therapeutic benefits.

#### 4. Conclusions

MgO nanoparticles were synthesized using a simple chemical method. The XRD spectrum demonstrated that the MgO nanoparticles exhibited a monoclinic structure. Furthermore, the XRD spectra confirmed the formation of MgO nanoparticles in a single phase. The smallest crystallite size, measuring 19.91 nm, was observed in the case of MgO nanoparticles. The purity of the MgO nanoparticles was also confirmed through FTIR analysis. Remarkably, the MgO nanoparticles exhibited excellent inhibition against various microorganisms, reaching their maximum inhibitory effect. To investigate the impact of scaffolds on bone repair, an animal model was established. The findings revealed that scaffolds exerted positive effects on bone remodeling, fixation, and the generation of new trabecular bone. Histological analyses indicated elevated levels of OCN and ALP at the site of bone damage following scaffold implantation, thereby promoting bone healing through enhanced trabecular bone formation, thickness, and connectivity. The molecular mechanisms underlying scaffold-induced bone healing may involve the modulation of ALP and OCN gene expression mediated by Runx2. Consequently, this research suggests that scaffolds could potentially offer clinical benefits in the treatment of bone abnormalities and fractures associated with osteoporosis.

License number for animal research facilities issued by Mustansiriyah University, College of Science, Department of Physics, at 2022 to Ministry of Health, National Center for Drug Control and Research (NCDRC), Iraq.

**Acknowledgement:** Author would like to thank dean of College of Science, Al-Nahrain University, Professor Dr. Asmaa Hadi Hohammed for supportive advice.

**Funding:** No funding was received for this research.

**Conflict of Interest:** Author declares no conflict of interest.

#### References

- [1] Dizaj, S.M.; Lotfipour, F.; Barzegar-Jalali, M.; Zarrintan, M.H.; Adibkia, K.; "Antimicrobial activity of the metals and metal oxide nanoparticles". *Mater. Sci. Eng. C. Mater. Biol. Appl.*, 44:278–84, 2014.
- [2] Hajipour, M.J.; Fromm, K.M.; Ashkarran, A.A.; Jimenez de Aberasturi, D.; de Larramendi, I.R. and Rojo, T.; et al.; 'Antibacterial properties of nanoparticles'. *Trends Biotechnol.*, 30(10):499–51, 2012.
- [3] Tang, Z.X. and Lv, B.F.; "MgO nanoparticles as antibacterial agent: preparation and activity". *Braz. J. Chem. Eng.*, 31(3):591–601, 2014.
- [4] Leung, Y.H.; Ng, A.M.; Xu, X.; Shen, Z.; Gethings, L.A. and Wong, M.T. et al.; "Mechanisms of antibacterial activity of MgO: non-ROS mediated toxicity of MgO nanoparticles towards *Escherichia coli*". *Nano. MicroSmall.* 10(6):1171–1183, 2014.
- [5] Li, X.; Robinson, S.M.; Gupta, A.; Saha, K.; Jiang, Z. and Moyano, D.F. et al.; "Functional gold nanoparticles as potent antimicrobial agents against multi-drug-resistant bacteria". *ACS Nano.*, 8 (10):10682–6, 2014
- [6] Tang, Z. X.; Fang, X. J.; Zhang, Z. L.; Zhou, T.; Zhang, X. Y. and Shi, L. E.; "Nanosize MgO as antibacterial agent: Preparation and characteristics". *Braz. J. Chem. Eng.*, 29 (4): 775-781, 2012.
- [7] Zhang, K.; An, Y.; Wang, F.; Lin, L. and Guo, H.; "Experimental investigation on water treatment by the combined nano MgO-nanofiltration technique". *Water Sci. Technol.*, 63 (11) :2542-2546, 2011.
- [8] Zhou, J.; Yang, S. and Yu, J.; "Facile fabrication of mesoporous MgO microspheres and their enhanced adsorption performance for phosphate from aqueous solutions". *Colloids Surf., A*, 379 (1-3) :102-108, 2011.
- [9] Huergo, L.F.; Rahman, H.; Ibrahimovic, A.; Day, C.J.; Korolik, V.; "Campylobacter jejuni Dps protein binds DNA in the presence of iron or hydrogen peroxide". *J. Bacteriol.*, 195(9):1970–8, 2013.
- [10] Kim, J.C.; Oh, E.; Kim, J.; Jeon, B.; "Regulation of oxidative stress resistance in *Campylobacter jejuni*, a microaerophilic foodborne pathogen". *Front Microbiol.*, 6:751, 2015.
- [11] Sood, R. and Chopra, D.S.; "Improved yield of green synthesized crystalline silver nanoparticles with potential antioxidant

- 
- activity". *Int. Res. J. Pharm*, 8(4):100-104, 2017.
- [12] Kong, F.; Wang, J.; Han, R.; Ji, S.; Yue, J.; Wang, Y. and Ma, L.; "Antifungal activity of magnesium oxide nanoparticles: effect on the growth and key virulence factors of *Candida albicans*". *Mycopathologia*, 185(3):485-494, 2020.
- [13] Rani, N.; Chahal, S.; Chauhan, A.S.; Kumar, P.; Shukla, R. and Singh, S.K.; "X-ray analysis of MgO nanoparticles by modified Scherer's Williamson-Hall and size-strain method". *Mater. Today: Proc.*, 12 (part 3):543-548, 2019.
- [14] Dobrucka, R.; "Synthesis of MgO nanoparticles using *Artemisia abrotanum* herba extract and Their antioxidant and photocatalytic properties". *Iranian J. Sci. Technol., Trans. A: Sci.*, 42(2):547-555, 2018.
- [15] Raghavendra, M.; Lalithamba, H.S.; Sharath, B.S. and Rajanaika, H.; "Synthesis of N<sub>2</sub>-protected formamides from amino acids using MgO nano catalyst: Study of molecular docking and antibacterial activity". *Int. J. Sci. Technol.*, 24(6): 3002-3013, 2017.
- [16] Nemade, K.R. and Waghuley, S.A.; "Synthesis of MgO nanoparticles by solvent mixed spray Pyrolysis technique for optical investigation". *Int. J. Met.*, 2014: 389416, 2014.
- [17] Sugirtha, P.; Divya, R.; Yedhukrishnan, R.; Suganthi, K.S.; Anusha, N.; Ponnusami, V. and Rajan, K.S.; "Green synthesis of magnesium oxide nanoparticles using brassica oleracea and Punica granatum peels and their anticancer and photocatalytic activity". *Asian J. Chem.*, 27(7): 2513, 2015.
- [18] Abdallah, Y.; Ogunyemi, S. O.; Abdelazez, A.; Zhang, M.; Hong, X. and Ibrahim, E. et al.; "The green synthesis of MgO nano-flowers using *Rosmarinus officinalis* L.(Rosemary) and the antibacterial activities against *Xanthomonas oryzae* pv *oryzae*". *BioMed Res. Int.*, 2019:5620989, 2019.